

**REAL-TIME UAV-BASED TRAFFIC STATE ESTIMATION FOR MULTI-REGIONAL
TRAFFIC NETWORKS**

Kyriacos Theocharides

PhD Student*

ktheoc01@ucy.ac.cy

Charalambos Menelaou, Ph.D.

Research Associate*

cmenel02@ucy.ac.cy

Yiolanda Englezou, Ph.D.

Research Associate/Marie-Curie Fellow*

englezou.yiolanda@ucy.ac.cy

Stelios Timotheou, Ph.D., Corresponding Author

Assistant Professor*

timotheou.stelios@ucy.ac.cy

*KIOS Research and Innovation Center of Excellence &

Department of Electrical and Computer Engineering

University of Cyprus

P.O.Box 20537

CY-1678 Nicosia

Cyprus

Fax: +357-22-893455

Submission Date: November 14, 2023

1 ABSTRACT

2 Traffic state estimation (TSE) is a challenging task due to the collection of sparse and noisy mea-
3 surements from fixed points in the traffic network. Recently, Unmanned Aerial Vehicles (UAVs)
4 have been used as an alternative to fixed sensors such as induction loops, as they are non-intrusive,
5 can observe any area of the traffic network on demand and provide accurate traffic density and
6 speed measurements. Our main contribution is the development of an optimization framework
7 where small parts of the traffic network are monitored by UAVs and accurate estimates of traffic
8 density and mean speeds for every region in the traffic network are returned in real-time. Assuming
9 regional-based traffic dynamics, a cyclical UAV flight path is defined for each region. One UAV is
10 assigned to each flight path and monitors a small area of the region below. The UAV-based traffic
11 measurements are expressed as moving averages to smooth out fluctuations in traffic density and
12 mean speed. A moving horizon optimization problem is formulated, which minimizes the estima-
13 tion and process errors over a moving time window. The problem is non-convex and challenging
14 to solve, due to the presence of non-linear traffic dynamics. By considering free-flow conditions,
15 the optimization problem is recast to a quadratic program that returns density estimations for each
16 region of the traffic network in real time. Simulation results compare our UAV framework to an al-
17 ternative, where the whole traffic network is monitored by UAVs. Both frameworks obtain similar
18 results, despite the alternative framework using more UAVs than our framework.

19
20 *Keywords:* traffic state estimation, regional traffic dynamics, UAV-based sensing architecture, vis-
21 iting area, moving average, moving horizon window, convex optimization, sparse and noisy traffic
22 measurements.

1. INTRODUCTION

Traffic state estimation (TSE) is critical for traffic planning, management and operations. It refers to the process of inferring traffic states (e.g traffic densities, flow rates and speeds) from a limited amount of noisy observed traffic data. This process depends on the estimation approach utilised for the task, the traffic flow models considered to describe the traffic dynamics and the available input data.

In its early stages of research, TSE mainly focused on freeways due to their modelling simplicity and importance in transportation networks (1). By developing traffic models such as the cell transmission model and placing loop detectors at set points on the freeway, traffic states were accurately estimated at points between the loop detectors (2). Promising results from similar studies were also achieved with the use of dual loop detectors for travel time estimation (3), road-side cameras for speed estimation (4) and extended Kalman filters for traffic flow, mean speed, and density estimation (5).

Achieving accurate TSE of a large urban area is an expensive process if only stationary equipment such as loop detectors, cameras, and radars are used due to their high life cycle costs. These can range from \$20,000 per loop detector to \$75,000 per camera and include the initial cost of equipment, annual maintenance cost and replacement cost after a 10 year period (6). Stationary sensors also cause traffic disruption during installation and maintenance, resulting in further congestion and delays for road users. As a result, TSE of urban road networks has shifted to include data from mobile sensors, as these are non-intrusive, i.e cause no disruption to the road network as no installation and on-site maintenance is required. Examples of TSE of urban areas with mobile sensors include: loop detectors with GPS-enabled probe vehicles (7), loop detectors with GPS and Bluetooth devices (8), GPS-enabled probe vehicles (9) and GPS-enabled mobile phones (10).

Unmanned Aerial Vehicles (UAVs) have recently received attention as mobile sensors for traffic monitoring purposes (11). Autonomous UAVs in particular pose a number of advantages over fixed sensors, making them desirable for TSE:

1. A UAV flying at the maximum flight height of an urban area has a far superior field of view to a fixed sensor (e.g loop detector, fixed camera, radar etc). By following a pre-determined flight path, a UAV can cover a large section of a traffic network within a discrete time-step. Monitoring the same area using fixed sensors alone would require multiple sensors, thereby increasing costs and complexity.
2. A UAV costs less and is much easier to maintain or operate than a fixed sensor and is non-intrusive, i.e. it does not disrupt the flow of traffic due to installation/maintenance (12). This is especially useful in developing countries, which may not have the funds or existing infrastructure to use fixed sensors for TSE.
3. Computer vision algorithms used to analyse UAV video feed such as k-means clustering (13), convolutional neural networks (14), and YOLO object detectors (15), (16) can accurately detect the number of vehicles in a road, the length of a queue of vehicles, speed and trajectory of each vehicle, lane crossing of each vehicle and type of each vehicle. This level of detail is far superior to most types of common fixed-location sensors and provides a greater insight into traffic behaviour, allowing for more accurate TSE to be implemented. Even if such algorithms were implemented on fixed cameras, the level of detail would still be inferior to UAVs as they can monitor a much larger area at any given time from a bird's eye view.
4. UAVs can dynamically change their flight path to observe areas of high importance.

This is extremely useful as traffic demand is not always consistent from day to day and different areas of the traffic network may become congested at different times and under different circumstances (i.e a large event finishing, road works occurring, a natural disaster occurring). UAVs have the ability to rapidly respond to outliers and identify and observe critical areas of the traffic network with the goal of relieving congestion.

Although UAVs pose a number of advantages over fixed sensors, this does not imply that all fixed sensors should be replaced by UAVs. It may be advantageous in fact to combine real-time UAV measurements with measurements from fixed-location sensors if such sensors already exist in the traffic network. For example, fixed-location sensors could be used to measure main roads and UAVs could be used to dynamically respond to areas of congestion or unforeseen events e.g., traffic accidents, natural disasters etc. For the purpose of this work however, we focus on real-time measurements provided only by UAVs.

Real-time traffic monitoring of a large urban area can be achieved by flying a swarm of UAVs over a road network. This idea has been studied, with a data processing framework being proposed by Wu et al. (17) and simulations conducted by Garcia-Aunon, Roldan & Barrientos (18), while Elloumi et al. (19) have proposed effective methods and formations for UAV swarms to maximise their exposure to high-density traffic. To the knowledge of the authors, only Barmounakis & Geroliminis (20) have conducted a full-scale experiment involving a swarm of UAVs for traffic monitoring over a 1.3 km^2 area of Athens, Greece. Theoretically, an entire traffic network could be monitored by a swarm of UAVs, although this would require a large number of UAVs to monitor the road network, even for a small town (21). An alternative is to use a smaller swarm of UAVs and infer unobserved areas of the traffic network through TSE. A simulation-based work investigated the problem of traffic origin-destination matrix estimation using a swarm of UAVs and showed that UAV-based estimation yields 10 times better performance compared to traditional sensing (22). Recently, a Gaussian process interpolation framework was also proposed aiming to derive fine-grained traffic density estimations of distinct road segments in an offline Bayesian framework both under free-flow and congested conditions using only measurements obtained by UAVs (23).

In this work, we propose a novel optimization framework that achieves real-time TSE of an urban traffic network using measurements obtained only by UAVs which act as mobile sensors. We consider an urban network split into homogeneous regions where traffic dynamics are defined by a triangular macroscopic fundamental diagram (MFD) that describes the outflow of a region as a function of its density. A single UAV is assigned to each region and follows a cyclical, pre-determined flight path that covers the entire region. At each time-step, the UAVs collect vehicle density and mean speed measurements over a small area (known as a visiting area) of each region, subject to Gaussian noise. To obtain accurate estimates of regional densities and speeds at each time-step and for every region, an optimization problem based on regional traffic dynamics is formulated, which minimizes the estimation and process errors over a moving horizon window with the UAV-obtained measurements as inputs. The problem is non-convex and challenging to solve, due to the presence of non-linear traffic dynamics. By considering free-flow conditions, the optimization problem is recast to a quadratic program that can be fast and reliably solved to yield density estimations for each region of the traffic network. Simulation results are obtained for a specific traffic network illustrating that the proposed approach yields accurate estimates of regional densities and speeds for the traffic network using only a small number of UAVs. At the time of writing, this is the only work that aims to achieve multi-regional TSE with measurements

1 obtained by a swarm of UAVs.

2 The remainder of the paper is organised as follows. Section 2 describes the UAV-based
3 sensing architecture, while Section 3 presents the regional traffic model. Section 4 defines the traf-
4 fic state estimation problem under consideration, while Section 5 develops the solution approach.
5 Section 6 presents the simulation experiments performed to evaluate the proposed methodology
6 assuming a free-flow scenario and Section 7 outlines the main conclusions and future directions of
7 this work. Last, all sets, constants and variables of this paper are summarised in the Appendix.

8 2. UAV-BASED SENSING ARCHITECTURE

9 Traffic flow modelling of individual roads is challenging as the variance in vehicle density can be
10 high even with adjacent roads, i.e., some roads may be very dense with traffic whereas adjacent
11 roads may be close to empty. This implies that when monitoring a specific length of road, con-
12 clusions cannot be drawn about adjacent roads which are not being monitored. To circumvent this
13 issue, a number of adjacent roads can be aggregated into a larger region such that the variance in
14 vehicle density is low (24). Because the variance in vehicle density is low, it can be said that such
15 aggregated regions are homogeneous, meaning that the traffic density of all roads in the region is
16 similar throughout space and time. Let $\mathcal{R} = \{1, 2, \dots, R\}$ is the set of all homogeneous regions in
17 a traffic network. A vehicle starts its journey from an origin region $o \in \mathcal{O}$ and finishes its journey
18 at a destination region $d \in \mathcal{D}$, where $\mathcal{O} \subseteq \mathcal{R}$ is the set of origin regions, and $\mathcal{D} \subseteq \mathcal{R}$ is the set
19 of destination regions; $O = |\mathcal{O}|$ and $D = |\mathcal{D}|$ denote the total number of origin and destination
20 regions. We define the set $\mathcal{T} = \{1, \dots, K\}$ where K is the total number of simulation time-steps,
21 each of duration T_s [hours].

22 A single UAV is assigned to each region $r \in \mathcal{R}$ and follows a flight path p_r flying at a height
23 of h [m]. Due to speed constraints of the UAV, it may be infeasible for a UAV to monitor the whole
24 of region r in one time-step $k \in \mathcal{T}$. To circumvent this issue, we partition each path p_r into sections
25 of equal length, denoted as p_r^m where $m \in \mathcal{M}_r$ is defined by the ordered set $\mathcal{M}_r = \{1, 2, \dots, |\mathcal{M}_r|\}$.
26 As such, a UAV monitors a path section p_r^m instead of the entire path p_r during a single time-step
27 $k \in \mathcal{T}$. The area monitored by the path section p_r^m at time-step k is known as a *visiting area*.

28 Fig. 1 is a visual representation of a hexagonal region $r \in \mathcal{R}$ divided into $|\mathcal{M}_r| = 6$ UAV
29 visiting areas, each denoted with a different colour. Without loss of generality, we represent each
30 region $r \in \mathcal{R}$ as a hexagon as it is the largest polygon which can be tiled without leaving any empty
31 space, making it useful for visually representing homogeneous regions of a traffic network (25).
32 The UAV assigned to the hexagonal region in Fig. 1 monitors a single visiting area over a discrete
33 time-step, transitioning to the next visiting area along path p_r with each subsequent time-step. For
34 example, visiting areas 1 and 2 (green and orange visiting areas) in Fig. 1 are observed by the UAV
35 at time steps $\{1, 7, 13, \dots\}$ and $\{2, 8, 14, \dots\}$, respectively. As such, the UAV in Fig. 1 completes 1 full
36 cycle of path p_r every 6 time-steps.

37 Let $\mathbf{m} = [1, 2, \dots, M_r]$ be a vector identical to the ordered set \mathcal{M}_r and let the constant $b =$
38 $\text{mod}(K, M_r)$. We define a vector \mathbf{c}_r as a column vector which maps every time-step $k \in \mathcal{T}$ to
39 visiting area $m \in \mathcal{M}_r$ inhabited by a UAV for every region $r \in \mathcal{R}$:

$$40 \quad \mathbf{c}_r = \underbrace{[\mathbf{m}, \mathbf{m}, \dots, \mathbf{m}]_{\text{floor}(\frac{K}{M_r})}}_{\text{floor}(\frac{K}{M_r})}, \mathbf{m}(1:b)]^T. \quad (1)$$

41 The UAVs have the ability to measure the *visiting area regional density*, $\tilde{\rho}_r^m(k)$ [veh/km]

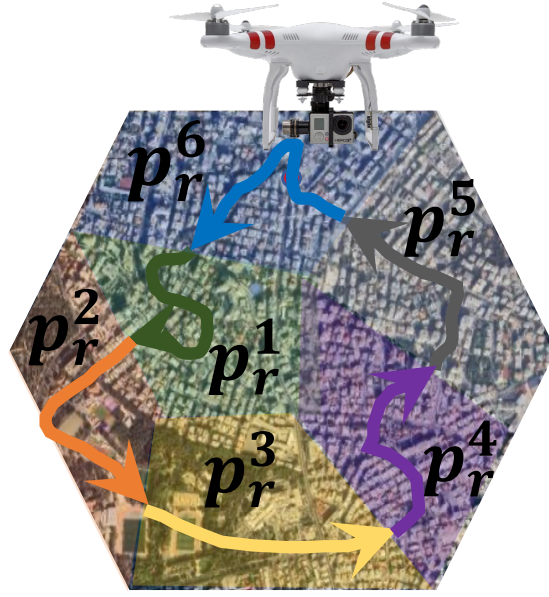


FIGURE 1: A homogeneous hexagonal urban region divided into six visiting areas with a pre-determined UAV flight path.

for a given visiting area $m \in \mathcal{M}_r$ for region $r \in \mathcal{R}$ and time-step $k \in \mathcal{T}$, subject to Gaussian noise. Each visiting area $m \in \mathcal{M}_r$ differs in topology and has slight variations in vehicle density and mean speed with other visiting areas $m \in \mathcal{M}_r$. As such, we cannot make the assumption that $\tilde{\rho}_r^m(k) = \tilde{\rho}_r(k)$ and (k), where $\tilde{\rho}_r(k)$ is the *measured vehicle density*.

To circumvent this problem, we express $\tilde{\rho}_r(k)$ as a moving average of the measurements $\tilde{\rho}_r^m$:

$$\tilde{\rho}_r(k) = \frac{1}{N} \sum_{n=0}^{N-1} \tilde{\rho}_r^{\mathbf{c}_r[k-n]}(k-n), \quad (2)$$

The summations occur over a moving window of N time-steps, beginning at time-step $k - N + 1$ up until the current time-step k . The visiting areas $m \in \mathcal{M}_r$ are related to the current time-step k by the vector \mathbf{c}_r at element k , denoted as $\mathbf{c}_r[k]$.

We assume that UAVs have a clear, unobstructed view of each visiting area $m \in \mathcal{M}_r, \forall k \in \mathcal{T}$. Moreover, it is assumed that once the UAV's battery is approaching empty, the UAV can land at pre-designated spots and have its battery swapped with a fully charged one, as was done in (20). The time taken to swap out a battery and resume flight is considered negligible, hence it is not factored into our simulation results. Although modern UAVs have flight times of roughly 30 minutes in ideal conditions, it is possible that UAVs with flight times of a few hours may be commercialised in the future (26), such that UAV battery swapping may become less frequent.

The proposed UAV architecture utilises the maneuverability that multi-rotor UAVs have over other mobile sensors. As UAVs are airborne, they can monitor far more spatial traffic information than mobile sensors such as probe vehicles and GPS enabled phones. Moreover, because they are not constrained by roads and vehicle congestion, they can traverse larger distances over a shorter period of time compared to other mobile sensors. As such, $\tilde{\rho}_r(k)$ can be obtained by monitoring a succession of small visiting areas $m \in \mathcal{M}_r$ and using a moving average of the mea-

surements $\tilde{\rho}_r^m(k)$. Since only one UAV is required per region $r \in \mathcal{R}$, the proposed UAV-based sensing architecture is far more cost effective than other mobile sensor based methods as less sensors are required and less personnel is needed to operate each sensor. Lastly, due to the availability of UAVs and UAV trained pilots, this architecture can be applied over any urban area, so long as the maximum height of the buildings in the urban area does not exceed the h , the flight height of the UAVs.

3. REGIONAL TRAFFIC MODEL

Let $q_r(k)$ [veh/h] be the *intended vehicle outflow* at time-step $k \in \mathcal{T}$ for region $r \in \mathcal{R}$ given as the product of the region density $\rho_r(k)$ [veh/km] and speed $u_r(k)$ [km/h] at time-step k , i.e $q_r(k) = \rho_r(k)u_r(k)$. The MFD expresses $q_r(k)$ as a piecewise function of $\rho_r(k)$, given by

$$q_r(k) = \begin{cases} q_r^C \left(\frac{\rho_r(k)}{\rho_r^C} \right) & 0 \leq \rho_r(k) < \rho_r^C, \\ q_r^C \left(\frac{\rho_r^J - \rho_r(k)}{\rho_r^J - \rho_r^C} \right) & \text{otherwise,} \end{cases} \quad (3)$$

where q_r^C is the maximum vehicle outflow, ρ_r^C the critical density and ρ_r^J the jam density. Maximum vehicle outflow q_r^C occurs when $\rho_r = \rho_r^C$, while $q_r = 0$ occurs at the jam density $\rho_r = \rho_r^J$ for $r \in \mathcal{R}$. When traffic density takes in values of $0 \leq \rho_r(k) < \rho_r^C$ the network operates under free-flow (uncongested) conditions, while if $\rho_r^C \leq \rho_r(k) \leq \rho_r^J$ the network operates under congestion. Note that when $\rho_r \leq \rho_r^C$, the average speed of region $r \in \mathcal{R}$ is the free-flow speed u_r^f [km/h] $\forall r \in \mathcal{R}$.

Let $\rho_{rd}(k)$ be the density of vehicles in region $r \in \mathcal{R}$ with final destination region $d \in \mathcal{D}$ at time-step k . Similarly, let $q_{rd}(k)$ be an intended vehicle transfer flow from region $r \in \mathcal{R}$ to destination region $d \in \mathcal{D}$, such that $q_{rd}(k) = \rho_{rd}(k)u_r(k)$. These are expressed by:

$$\rho_r(k) = \sum_{d \in \mathcal{D}} \rho_{rd}(k), \quad (4)$$

$$q_r(k) = \sum_{d \in \mathcal{D}} q_{rd}(k). \quad (5)$$

Let \mathcal{J}_r^- be the set of regions which directly neighbour region $r \in \mathcal{R}$ and let \mathcal{J}_r^+ be the set of regions which directly neighbour region $r \in \mathcal{R}$ but include region r such that $\mathcal{J}_r^+ = \mathcal{J}_r^- \cup \{r\}$. The set \mathcal{J}_r is defined as:

$$\mathcal{J}_r = \begin{cases} \mathcal{J}_r^+ & \text{if } r \in \mathcal{D}, \\ \mathcal{J}_r^- & \text{if } r \notin \mathcal{D}. \end{cases} \quad (6)$$

Note that, vehicles entering and exiting region $r \in \mathcal{R}$ can only do so via region j , where $j \in \mathcal{J}_r$.

Let $\rho_{rjd}(k)$ be the density of vehicles in region $r \in \mathcal{R}$ with final destination $d \in \mathcal{D}$ through neighbouring region $j \in \mathcal{J}$ at time-step k . Likewise, let $q_{rjd}(k)$ be the intended vehicle transfer flow from region $r \in \mathcal{R}$ to destination region $d \in \mathcal{D}$ through neighbouring region $j \in \mathcal{J}_r$ at time-step k . Terms $\rho_{rd}(k), \rho_{rjd}(k), q_{rd}(k), q_{rjd}(k)$ are related by:

$$q_{rd}(k) = \sum_{j \in \mathcal{J}_r} q_{rjd}(k), \quad (7)$$

$$\rho_{rd}(k) = \sum_{j \in \mathcal{J}_r} \rho_{rjd}(k). \quad (8)$$

Note that if $r = j = d$, the vehicle is in its destination region $d \in \mathcal{D}$ and will exit the traffic

1 network and the *vehicle exit flow* $q_{ddd}(k)$ applies. In addition $q_{djd}(k) = 0$ where $j \in \mathcal{J}_r^-$, hence
 2 $q_{dd}(k) = q_{ddd}(k)$.

3 The *interboundary flow capacity* $C_{rj}(\rho_j(k))$ [veh/h], determines the rate at which vehicles
 4 can enter a neighbouring region $j \in \mathcal{J}_r^-$ from $r \in \mathcal{R}$, and is a piecewise function of $\rho_j(k)$ with
 5 two pieces (i) a constant value C_{rj}^{MAX} [veh/h], and (ii) a decreasing, linear function of $\rho_j(k)$:

$$6 \quad C_{rj}(\rho_j(k)) = \begin{cases} C_{rj}^{MAX} & \text{if } 0 \leq \rho_j(k) < \beta \rho_j^J, \\ \frac{C_{rj}^{MAX}}{1-\beta} \left(1 - \frac{\rho_j(k)}{\rho_j^J}\right) & \text{otherwise.} \end{cases} \quad (9)$$

7 The term C_{rj}^{MAX} [veh/h] is the *maximum interboundary flow capacity* from $r \in \mathcal{R}$ to $j \in \mathcal{J}$
 8 and $0 < \beta < 1$ is a parameter that defines the point where inter boundary capacity starts to decrease
 9 (27).

10 The *actual vehicle transfer flow* from $r \in \mathcal{R}$ to destination $d \in \mathcal{D}$ through neighbouring
 11 region $j \in \mathcal{J}_r$ is defined as:

$$12 \quad c_{rjd}(k) = \min \left(q_{rjd}(k), C_{rj}(\rho_j(k)) \frac{q_{rjd}(k)}{\sum_{d' \in \mathcal{D}} q_{rjd'}(k)} \right). \quad (10)$$

13 As shown above, $c_{rjd}(k)$ is the minimum of two terms (i) an intended vehicle transfer flow
 14 $q_{rjd}(k)$, from region $r \in \mathcal{R}$ to the next neighbouring region $j \in \mathcal{J}_r$ and destination region $d \in \mathcal{D}$,
 15 (ii) the interboundary flow capacity between regions $r \in \mathcal{R}$ and $j \in \mathcal{J}_r$.

16 The term $c_{rj}(k)$ is expressed as a summation of $c_{rjd}(k)$ over the destination regions $d \in \mathcal{D}$:

$$17 \quad c_{rj}(k) = \sum_{d \in \mathcal{D}} c_{rjd}(k). \quad (11)$$

18 The *traffic conservation equation* computes $\rho_{rd}(k+1)$, and is expressed as:

$$19 \quad \rho_{rd}(k+1) = \rho_{rd}(k) + \frac{T_s}{l_r} \sum_{j \in \mathcal{J}_r} [c_{jrd}(k) - c_{rjd}(k)] + \frac{1}{l_r} D_{rd}(k), \quad (12)$$

20 where T_s is the simulation time-step, $D_{rd}(k)$ is the number of vehicles entering the network from
 21 region $r \in \mathcal{R}$ during time-step $k \in \mathcal{T}$ destined to region $d \in \mathcal{D}$ and l_r [km] is the *average road*
 22 *length* of region $r \in \mathcal{R}$. Note that l_r is chosen such that it satisfies the Courant-Friedrichs-Lewy
 23 condition (28), hence we have that $T_s \leq l_r \setminus u_r^f$.

24 4. PROBLEM STATEMENT

25 The measured parameters $\tilde{\rho}_r(k)$ and $\tilde{u}_r(k)$ defined in Section 2 are subjected to Gaussian mea-
 26 surement noise from the UAV and process noise, i.e the noise between the traffic model described
 27 in Section 3 and the actual vehicle dynamics in real urban areas. To minimize these errors, we
 28 develop a novel optimization problem with inputs the noisy measurements from the UAVs $\tilde{\rho}_r(k)$,
 29 $\tilde{u}_r(k)$ and outputs *estimated regional densities* $\hat{\rho}_r(k)$, $\hat{\rho}_{rd}(k)$, $\forall k \in \mathcal{T}$, $\forall r \in \mathcal{R}$, $\forall d \in \mathcal{D}$. The aim
 30 is to achieve values of $\hat{\rho}_r(k)$, $\hat{\rho}_{rd}(k)$, which are as close as possible to the *true regional densities*
 31 $\rho_r(k)$, $\rho_{rd}(k)$.

32 We define the *estimation errors* $v_r^p(k)$, $v_r^u(k)$, as the difference between $\hat{\rho}_r(k)$, $\hat{u}_r(k)$, and
 33 the *measured regional parameters* $\tilde{\rho}_r(k)$, $\tilde{u}_r(k)$, $\forall k \in \mathcal{T}$, $\forall r \in \mathcal{R}$:

$$\begin{bmatrix} \hat{\rho}_r(k) \\ \hat{u}_r(k) \end{bmatrix} - \begin{bmatrix} \tilde{\rho}_r(k) \\ \tilde{u}_r(k) \end{bmatrix} = \begin{bmatrix} v_r^p(k) \\ v_r^u(k) \end{bmatrix}. \quad (13)$$

The parameters $v_r^p(k), v_r^u(k)$ follow a normal distribution such that $v_r^p(k) \sim \mathcal{N}(\mu_p, \sigma_p^2)$, $v_r^u(k) \sim \mathcal{N}(\mu_u, \sigma_u^2)$, where $\mu_p = \mu_u = 0$. Vector forms of these quantities are denoted as $\hat{\rho}(k), \tilde{\rho}(k), \hat{u}(k), \tilde{u}(k), v^p(k), v^u(k) \in \mathbb{R}^{R \times 1}$.

We define the *estimated traffic conservation equation*, given by:

$$\hat{\rho}_{rd}(k+1) = \hat{\rho}_{rd}(k) + \frac{T_s}{l_r} \sum_{j \in \mathcal{J}_r} [\hat{c}_{jrd}(k) - \hat{c}_{rjd}(k)] + \frac{1}{l_r} D_{rd}(k) + w_{rd}^p(k). \quad (14)$$

The above equation is identical to the *traffic conservation equation* (12) with the addition of the *process error* $w_{rd}^p(k)$, where $w_{rd}^p(k) \sim \mathcal{N}(\mu_w, \sigma_w^2)$, $\mu_w = 0$.

We formulate the problem of finding the best estimates of $\hat{\rho}_r(k), \hat{\rho}_{rd}(k)$ as a least squares minimization problem. We employ a moving horizon window of fixed length W looking into the past, such that $\mathcal{K}_{k-W+1}^k = \{k-W+1, k-W+2, \dots, k\}$ denotes the time window considered at time-step k .

The minimization routine aims to find an optimal solution that minimises the estimation errors $v_r^p(k), v_r^u(k)$ and process errors $w_{rd}^p(k)$ for the whole of the moving horizon window. The estimation and process errors $v_r^p(k), v_r^u(k), w_{rd}^p(k)$ for time-step k are expressed as a single column vector \mathbf{e}_k :

$$\mathbf{e}_k = [v_r^p(k), v_r^u(k), w_{rd}^p(k)]^T, \quad (15)$$

where $\forall r \in \mathcal{R}, \forall d \in \mathcal{D}, \forall k \in \mathcal{K}_{k-W+1}^k$.

The optimisation problem referred to as P1, is defined by:

$$\underset{\mathbf{e}_k}{\text{minimize}} \quad \sum_{k \in \mathcal{K}_{k-W+1}^k} \mathbf{e}_k^T \mathbf{Q}_k^{-1} \mathbf{e}_k \quad (16a)$$

subject to Traffic Dynamics: (3) – (11), (13) – (15),

$$0 \leq \hat{\rho}_r(k) \leq \rho_r^J \quad r \in \mathcal{R}, k \in \mathcal{K}_{k-W+1}^k, \quad (16b)$$

$$0 \leq \hat{q}_r(k) \leq q_r^C \quad r \in \mathcal{R}, k \in \mathcal{K}_{k-W+1}^k, \quad (16c)$$

$$0 \leq \hat{u}_r(k) \leq u_r^f \quad r \in \mathcal{R}, k \in \mathcal{K}_{k-W+1}^k, \quad (16d)$$

$$\hat{q}_r(k) = \hat{\rho}_r(k) \hat{u}_r(k) \quad r \in \mathcal{R}, k \in \mathcal{K}_{k-W+1}^k, \quad (16e)$$

$$\hat{q}_{rd}(k) = \hat{\rho}_{rd}(k) \hat{u}_r(k) \quad r \in \mathcal{R}, d \in \mathcal{D}, k \in \mathcal{K}_{k-W+1}^k, \quad (16f)$$

$$\hat{q}_{rjd}(k) = \hat{\rho}_{rjd}(k) \hat{u}_r(k) \quad r \in \mathcal{R}, d \in \mathcal{D}, k \in \mathcal{K}_{k-W+1}^k, \quad (16g)$$

Variables: $\hat{\rho}_{rjd}(k), \hat{q}_{rjd}(k), \hat{c}_{rjd}(k), \hat{u}_r(k), v_r^p(k), v_r^u(k), w_{rd}^p(k)$.

Eq. (16a) is the objective function to be minimised, given as the sum of squared errors defined by Eq. (15), where the matrix \mathbf{Q}_k is the covariance matrix of the error vector \mathbf{e}_k . The errors are minimised over the entire moving horizon window $k \in \mathcal{K}_{k-W+1}^k$. Constraints (3) – (11), (13) – (15) are the traffic dynamics, while inequalities (16b) – (16d) impose physical constraints on the variables $\hat{\rho}_r(k), \hat{q}_r(k), \hat{u}_r(k)$ and (16e) – (16f) compute $\hat{q}_r(k)$ and $\hat{q}_{rd}(k)$.

Note that P1 is nonconvex and therefore nonlinear due to constraints (3), (9), (10), (16e), (16f). For the problem to converge to a global minimum, the constraints must be linearised such that the problem becomes convex.

5. SOLUTION APPROACH

In this section, we develop a solution approach to problem P1 under free-flow conditions, i.e., considering that $\rho_r(k) \leq \min(\rho_r^C, \beta \rho_r^J), \forall r \in \mathcal{R}, k \in \mathcal{K}_1^K$. We consider TSE in free-flow conditions as some traffic control strategies primarily focus on maintaining free-flow conditions to maximize traffic throughput (29), (30), (31), (32), (33). Such strategies are employed before the traffic network reaches a congested state and therefore require accurate regional density values ρ_r in real-time to be effective. Hence, we limit the focus of our study to free-flow conditions only.

Under free-flow conditions, it is true that $u_r(k) = u_r^f$ such that the MFD relationship (3) is simplified to

$$q_r(k) = \rho_r(k)u_r^f. \quad (17)$$

In a similar way, the nonlinear constraints $q_{rd}(k) = \rho_{rd}(k)u_r(k)$ and $q_{rjd}(k) = \rho_{rjd}(k)u_r(k)$ are changed into the linear constraints:

$$q_{rd}(k) = \rho_{rd}(k)u_r^f, \quad (18)$$

$$q_{rjd}(k) = \rho_{rjd}(k)u_r^f. \quad (19)$$

Under free-flow conditions it is also true that $C_{rj}(\rho_j(k)) = C_{rj}^{MAX}$. Hence, Eqs. (10) can be simplified into the following inequality constraints:

$$c_{rjd}(k) = q_{rjd}(k), \quad (20)$$

$$\sum_{d \in \mathcal{D}} c_{rjd}(k) \leq C_{rj}^{MAX}, \quad (21)$$

Following the re-formulations of the non-linear constraints, the linear minimization problem P2 is defined by:

$$\underset{\mathbf{e}_k}{\text{minimize}} \quad \sum_{k \in \mathcal{K}_{k-W+1}^k} \mathbf{e}_k^T \mathbf{Q}_k^{-1} \mathbf{e}_k \quad (22a)$$

subject to Traffic Dynamics: (4) – (8), (11), (13) – (15), (17) – (19), (20), (21),

$$0 \leq \hat{\rho}_r(k) \leq \rho_r^C \quad r \in \mathcal{R}, k \in \mathcal{K}_{k-W+1}^k, \quad (22b)$$

$$0 \leq \hat{q}_r(k) \leq q_r^C \quad r \in \mathcal{R}, k \in \mathcal{K}_{k-W+1}^k, \quad (22c)$$

Variables: $\hat{\rho}_{rjd}(k), \hat{q}_{rjd}(k), \hat{c}_{rjd}(k), v_r^p(k), v_r^u(k), w_{rd}^p(k)$.

Problem P2 is identical to P1, but with all non-linear constraints relaxed to form a completely linear (hence convex) optimisation problem. We solve P2 at every time-step $k \in \mathcal{T}$ to obtain the best estimates of $\hat{\rho}_r(k), \hat{\rho}_{rd}(k)$.

6. SIMULATION RESULTS

We assume an urban traffic network, which we split into $R = 7$ homogeneous regions, where each region $r \in \mathcal{R}$ can be both an origin and destination region, hence $\mathcal{R} \equiv \mathcal{O} \equiv \mathcal{D}$. The length of each region $r \in \{1, 2, \dots, 7\}$ is set to $[2, 4, 3, 2, 3, 5, 4]$ km, respectively. We assume also that each

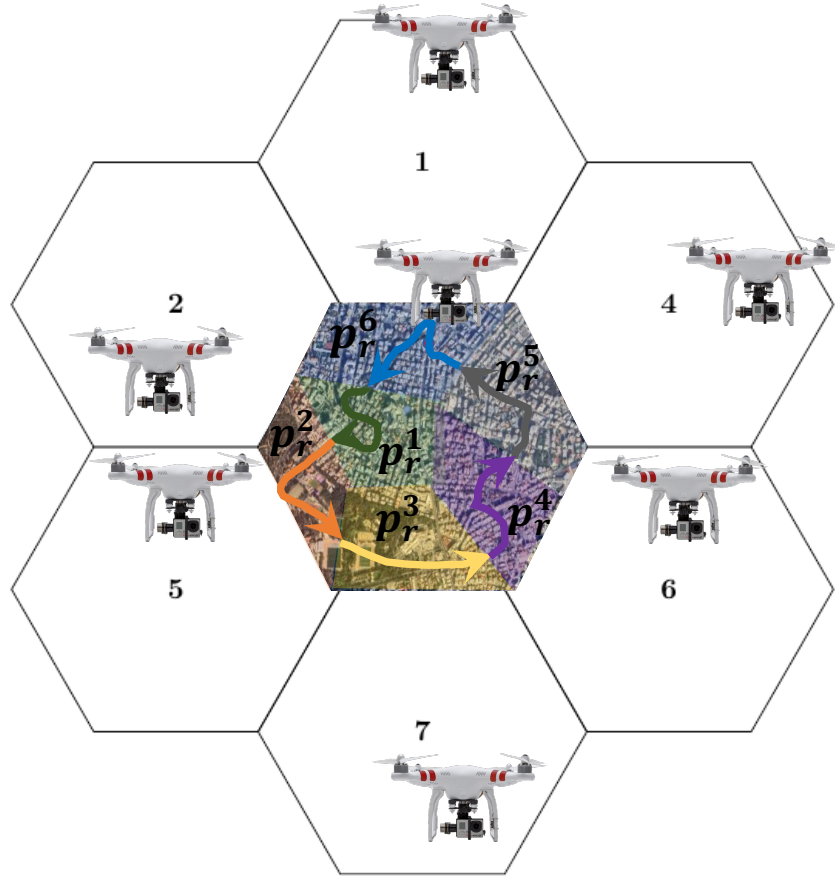


FIGURE 2: Urban traffic network split into seven hexagonal regions where a UAV is monitoring each region. Region $r = 3$ (centre) shows the six visiting areas that contain the pre-determined flight path of the UAV.

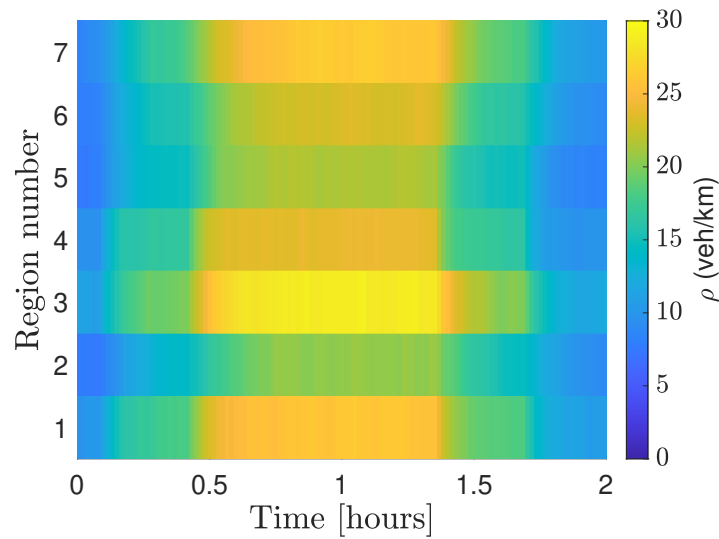


FIGURE 3: Space-time graph of the regional density $\rho_r(k)$ due to traffic demand, averaged over 10 simulations.

1 region is split into $M_r = 6$ visiting areas, where $r \in \mathcal{R}$. Fig. 2 shows a visual representation of the
 2 traffic network, where visiting areas $m \in \mathcal{M}_r$ are shown for region $r = 3$ only. We assume: $\rho_r^C =$
 3 30 veh/km, $\rho_r^J = 130$ veh/km, $q_r^C = 1500$ veh/h, $C_{rj}^{MAX} = 1500$ veh/h, $u_r^f = 50$ km/h, $\beta = \frac{\rho_r^C}{\rho_r^J}$ and
 4 $T_s = 60s$.

5 The simulation represents a medium demand, free-flow scenario where peak densities are
 6 close to the critical density $\rho_r^C = 30$ veh/km and the total simulation runtime is $K = 120$ time-steps,
 7 hence $T = 2$ hours. The vehicle demand for the traffic network is dictated by the origin-destination
 8 matrix \mathbf{D} . The demand increases linearly up until time-step $k = 40$, held constant until time-
 9 step $k = 70$ and linearly decreases until time-step $k = 120$, the end of the simulation. As shown
 10 in Fig. 3, peak density for all regions occurs around the 1 hour mark. For simulations where
 11 $\rho_r(k) \leq \rho_r^C, \forall r \in \mathcal{R}, \forall k \in \mathcal{T}$, Eqs. 17 - 19 & 20 are changed from inequalities to equalities, as all
 12 of the intended vehicle outflow $q_r(k)$ is modelled by the free-flow section of the MFD.

13 Two UAV sensing architectures were simulated. The first is the architecture proposed in
 14 Section 2, with the moving average window set to $N = 6$ and is therefore known as UAV architec-
 15 ture 1. The second UAV-based sensing architecture places a single UAV in every visiting area m
 16 and each UAV stays along the path p_r^m , rather than cycling across the whole path p_r and is known
 17 as UAV architecture 2. Evidently, UAV architecture 2 is more expensive and requires more pro-
 18 cessing power as it contains 6 times the number of UAVs compared to UAV architecture 1, but is
 19 expected to be more accurate as $\rho_r^m(k)$ and $u_r^m(k)$ are monitored and updated for $\forall r \in \mathcal{R}, \forall m \in \mathcal{M}$,
 20 $\forall k \in \mathcal{T}$. The UAV flight height h is set to 150 m to provide a large field of view without compro-
 21 mising the effectiveness of the traffic monitoring algorithm (34). For both simulations, the length
 22 of the moving horizon window W is set to 20 time-steps.

23 The process and measurement errors at every time-step $k \in \mathcal{T}$ are minimized over the
 24 moving horizon window W using optimization problem P2. For the solution of problem P2 the
 25 barrier method of Gurobi was used; the optimization problem is solved in under 2 seconds in about
 26 30 iterations. The simulation experiment is run 10 times with a demand scenario that yields the
 27 regional density shown in Fig. 3, and the estimated values of $\hat{\rho}_r(k)$ and $\hat{\rho}_{rd}(k)$ are averaged $\forall k \in \mathcal{T}$
 28 for the 10 different runs of the experiment. We calculate the R^2 given by:

$$29 \quad R^2 = 1 - \frac{\sum_{i=1}^{KR} (\rho_i - \hat{\rho}_i)^2}{\sum_{i=1}^{KR} (\rho_i - \bar{\rho}_i)^2}, \quad (23)$$

30 and the root mean square error (RMSE), which measures the magnitude of errors between
 31 the true values ρ_i and the estimated $\hat{\rho}_i$, given by:

$$32 \quad RMSE = \sqrt{\frac{\sum_{i=1}^{KR} (\rho_i - \hat{\rho}_i)^2}{KR}}. \quad (24)$$

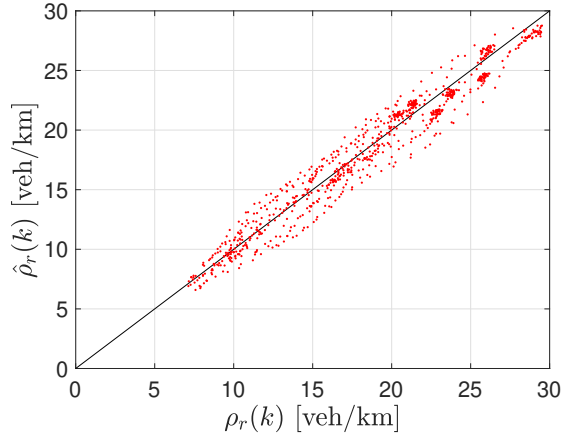
33 In Eqs. (23)-(25), $\rho_i = \rho_r(k)$, $\hat{\rho}_i = \hat{\rho}_r(k)$ and $\bar{\rho}_i = \bar{\rho}_r(k)$, where $\bar{\rho}_r(k)$ is the average value
 34 of $\rho_r(k), \forall r \in \mathcal{R}, \forall k \in \mathcal{T}$, for calculations involving $\rho_r(k)$. The mean average percentage error
 35 (MAPE) measures the average magnitude of error between the true values ρ_i and estimated $\hat{\rho}_i$ as a
 36 percentage, given by:

$$37 \quad MAPE = \frac{100}{KR} \sum_{i=1}^{KR} \frac{|\rho_i - \hat{\rho}_i|}{\rho_i}. \quad (25)$$

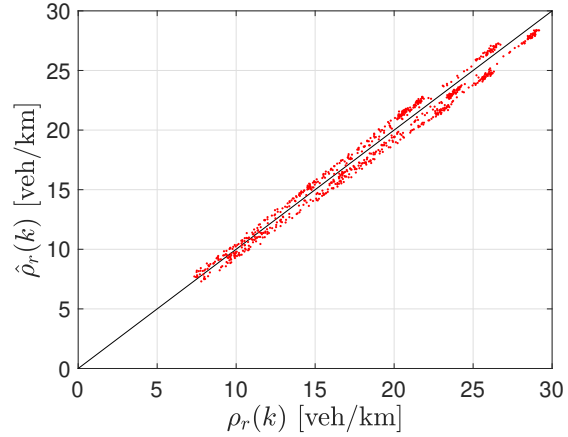
38 Note that for MAPE calculations, ρ_i and $\hat{\rho}_i$ values less than 1 veh/km were not included as

TABLE 1: Results for Both UAV-Based Sensing Architectures

UAV sensing architecture	Parameter	R^2	RMSE	MAPE (%)	Error Range
1	ρ_r	0.957	1.19	5.8	[-2.5,3.6]
	ρ_{rd}	0.971	0.58	12.6	[-2.5,4.5]
2	ρ_r	0.983	0.74	3.9	[-1.3,1.7]
	ρ_{rd}	0.976	0.52	12.2	[-1.7,3.0]



(a) UAV architecture 1



(b) UAV architecture 2

FIGURE 4: Plot of averaged $\hat{\rho}_r(k)$ vs $\rho_r(k)$ for both UAV-based sensing architectures.

1 small values that differ slightly can lead to high MAPE errors. The results for both UAV architec-
2 tures are shown in Table 1.

3 Fig. 4a and 4b plot the estimated regional density $\hat{\rho}_r(k)$ against the true density $\rho_r(k)$
4 from the simulation for UAV sensing architectures 1 and 2 respectively. The R^2 value for UAV
5 architecture 1 is 0.957, while for UAV architecture 2 it is 0.983, a 2.7% increase. Both R^2 values
6 are close to 1, indicating a strong correlation between $\hat{\rho}_r(k)$ and $\rho_r(k)$. As expected, the R^2 for
7 UAV architecture 2 is greater than that of UAV architecture 1, although the percentage difference
8 is not particularly high. The high accuracy of the estimated parameters is also shown by the low
9 RMSEs which are 1.19 veh/km and 0.74 veh/km respectively for UAV architectures 1 and 2. The
10 RMSE for UAV architecture 2 is 37.8% lower than UAV architecture 1, as the values of $\hat{\rho}_r(k)$
11 and $\rho_r(k)$ have a lower variance, which can be verified visually by inspecting Fig. 4a and 4b. The
12 MAPE also suggests that UAV architecture 2 is more accurate than UAV architecture 1 with MAPE
13 values of 3.9% and 5.8%, respectively. The MAPE of UAV architecture 2 is 32.8% lower than UAV
14 architecture 1, which is similar to the difference in RMSE values between the two architectures.

15 Fig. 5a and 5b plot the difference between ρ_r and $\hat{\rho}_r$ as a colourmap. The error range of
16 estimated densities $\hat{\rho}_r(k)$ for UAV architecture 1 is [-2.5,3.6] veh/km, whereas for UAV architecture
17 2 it is [-1.3,1.7] veh/km. The ranges for UAV architecture 1 are greater, which is expected given
18 that the RMSE is greater and the R^2 lower for UAV architecture 1 compared to UAV architecture
19 2. For UAV architecture 1, the maximum deviations occur around the 0.25, 0.5, 1.5 and 1.75 hour
20 mark, as shown in Fig. 5a. This can be explained by the traffic demand increasing sharply at times

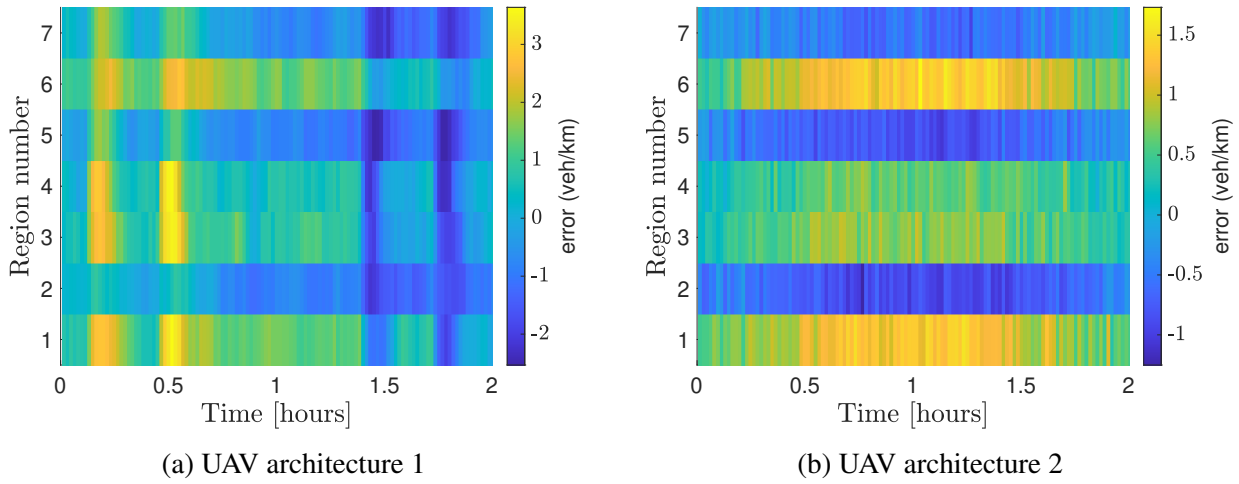


FIGURE 5: Space-time graph of $\rho_r(k) - \hat{\rho}_r(k)$ for both UAV-based sensing architectures.

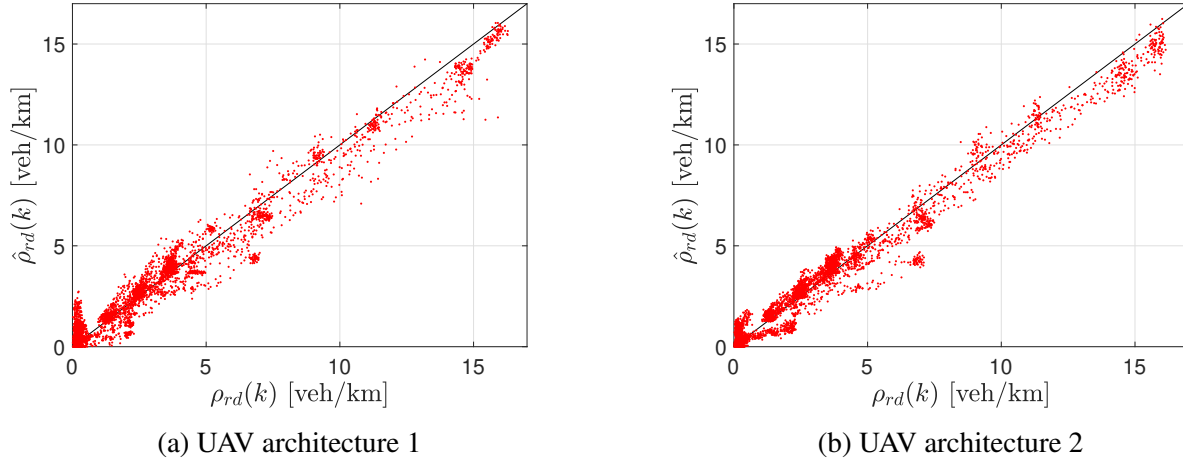


FIGURE 6: Plot of averaged $\hat{\rho}_{rd}(k)$ vs $\rho_{rd}(k)$ for both UAV-based sensing architectures.

1 0.25 and 0.5 and then decreasing at times 1.5 and 1.75. Due to the nature of the moving average, the
 2 estimator does not react immediately to the changes in demand, hence it underestimates $\hat{\rho}_r$ before
 3 the 1 hour mark, and overestimates after. Note that this is not the case with UAV architecture 2,
 4 which updates $\tilde{\rho}_r^m(k)$ at every time-step $\forall k \in \mathcal{K}, \forall m \in \mathcal{M}, \forall r \in \mathcal{R}$. Fig. 5b indicates that the
 5 maximum deviations occur around the 1 hour mark, where traffic density is at its highest.

6 Values for $\rho_{rd}(k)$ can be estimated but not measured, as it is impossible for a UAV to
 7 identify the destination region $d \in \mathcal{D}$ for each vehicle in the traffic network. Having an accurate
 8 estimate $\hat{\rho}_{rd}(k)$ is useful for applying effective control laws to minimise congestion in the road
 9 network, although this is outside the scope of this work.

10 Fig. 6a and 6b plot $\hat{\rho}_{rd}(k)$ against $\rho_{rd}(k)$ for UAV sensing architectures 1 and 2 respec-
 11 tively. As was the case with the $\rho_r(k)$ values, the R^2 values are both close to 1 at 0.971 and 0.976
 12 respectively for UAV sensing architectures 1 and 2, indicating a very strong positive correlation.
 13 Moreover, the percentage difference between UAV sensing architectures 1 and 2 is very low at

0.5%, and is therefore considered negligible. This is because the majority of $\rho_{rd}(k)$ values are much lower than the $\rho_r(k)$, hence deviations are not so great, so $\hat{\rho}_{rd}(k) \approx \rho_{rd}(k)$ when $\rho_{rd}(k)$ is low. This is shown in Fig. 6a and 6b, where the majority of points lie close to the $\hat{\rho}_{rd}(k) = \rho_{rd}(k)$ line. Moreover, this explains the similarity of the RMSEs, which is 0.58 veh/km for UAV sensing architecture 1 and 0.52 for UAV sensing architecture 2, a 10.3 % decrease. The MAPE are relatively high for UAV sensing architectures 1 and 2 at 12.6% and 12.2% respectively. The reason for this is that unlike ρ_r , ρ_{rd} values cannot be measured by the UAV hence estimations are less accurate. Also, the values of ρ_{rd} are generally quite low, so small deviations result in a large MAPE. As expected, UAV architecture 2 is more accurate than UAV architecture 1 at estimating $\rho_{rd}(k)$, although it is only 3.2% more accurate. As expected, the error range between $\hat{\rho}_{rd}(k)$ and $\rho_{rd}(k)$ are greater for UAV sensing architecture 1 than UAV sensing architecture 2, with errors ranges [-2.5,4.5] veh/km and [-1.7,3.0] veh/km respectively.

Overall, UAV sensing architecture 2 produced higher R^2 values and lower RMSE, MAPE and deviations compared to UAV sensing architecture 1, as $\tilde{\rho}_r^m(k)$ was updated $\forall k \in \mathcal{T}, \forall m \in \mathcal{M}, \forall r \in \mathcal{R}$. In contrast, only one $\tilde{\rho}_r^m(k)$ was updated $\forall k \in \mathcal{T}, \forall r \in \mathcal{R}$ for UAV sensing architecture 1, as there is only 1 UAV per region r instead of 1 UAV per visiting area m . Despite this, the difference in R^2 values are very small if not negligible for $\hat{\rho}_r(k)$ and $\hat{\rho}_{rd}(k)$. The RMSE is 37.8 % lower for $\hat{\rho}_r(k)$ between UAV sensing architectures 1 and 2 and 10.3 % lower for $\hat{\rho}_{rd}(k)$. Similarly, the MAPE is 32.8 % lower for $\hat{\rho}_r(k)$ between UAV sensing architectures 1 and 2 and 3.2 % lower for $\hat{\rho}_{rd}(k)$. Given that UAV sensing architecture 2 requires 6 times more UAVs than UAV sensing architecture 1, this is considered a worthwhile trade-off, considering that all RMSEs are low and do not exceed 1.2 veh/km for any of the parameters. We have shown therefore through our simulations that our proposed UAV sensing architecture can obtain very respectable results while drastically reducing the number of UAVs and computational power needed by assigning 1 UAV per region r instead of 1 UAV per visiting area m .

7. CONCLUSIONS AND FUTURE WORK

This work proposes a novel optimization framework which returns accurate density and mean speed estimations of an urban traffic network in real-time through the use of real-time UAV data. Our proposed UAV architecture splits the traffic network into homogeneous regions where each region is further split into smaller visiting areas. The UAVs follow a pre-determined, cyclical flight path above each traffic region, observing a visiting area at each time-step. Noisy measurements of density and mean speed are obtained at every time-step for the visiting area being observed. Using these measurements as inputs, estimates for regional density, regional mean speed and regional densities with known destinations are obtained in real-time through a quadratic program solution approach which minimises estimation and process errors over a moving horizon with a moving average of measurements.

Our proposed UAV-based sensing architecture was compared to a benchmark architecture where each visiting area in the traffic network is constantly monitored by a UAV, i.e. full information of the traffic network is available for the benchmark architecture. Compared to this benchmark architecture, the proposed UAV sensing architecture produces high quality estimations of regional density and regional density with known destinations assuming a free-flow traffic scenario, despite the fact that the proposed architecture utilises six times less information obtained from the UAVs. We therefore conclude that full network traffic state estimation can be achieved using noisy UAV measurements from small parts of the traffic network under free-flow conditions. These findings

1 highlight the potential for UAV-based traffic state estimation as an accurate and affordable alterna-
2 tive to other sensing approaches for traffic monitoring and traffic state estimation such as stationary
3 or other mobile sensors.

4 Future research work includes a variety of vehicle demand scenarios (light/heavy conges-
5 tion), alternative UAV architectures and optimization frameworks and additional measurements
6 from UAVs (such as the transfer flows between regions) to increase estimation accuracy.

7 **ACKNOWLEDGEMENTS**

8 This work is supported by the European Union (i. ERC, URANUS, No. 101088124, ii. Hori-
9 zon 2020 Teaming, KIOS CoE, No. 739551 and iii. Marie Skłodowska-Curie IF project: BITS,
10 No. 101003435), and the Government of the Republic of Cyprus through the Deputy Ministry
11 of Research, Innovation, and Digital Strategy. Views and opinions expressed are however those
12 of the author(s) only and do not necessarily reflect those of the European Union or the European
13 Research Council Executive Agency. Neither the European Union nor the granting authority can
14 be held responsible for them.

15 **AUTHOR CONTRIBUTIONS**

16 The authors confirm contribution to the paper as follows: study conception and design: Kyriacos
17 Theocharides, Charalambos Menelaou, Yiolanda Englezou, Stelios Timotheou; data collection:
18 Kyriacos Theocharides; analysis and interpretation of results: Kyriacos Theocharides, Charalam-
19 bos Menelaou, Yiolanda Englezou; draft manuscript preparation: Kyriacos Theocharides, Char-
20 alambos Menelaou, Yiolanda Englezou, Stelios Timotheou. All authors reviewed the results and
21 approved the final version of the manuscript.

22 **DECLARATION OF CONFLICTING INTERESTS**

23 The author(s) declared no potential conflicts of interest with respect to the research, authorship,
24 and/or publication of this article.

1 **APPENDIX**

2 In this section we introduce all notations that are used in this paper. Table A1 shows all sets and
 3 constants and Table A2 describes all variables defined in this paper.

TABLE A1: Table of sets & constants.

Notation	Meaning
\mathcal{R}	Set of all homogeneous regions
\mathcal{O}	Set of all origin regions
\mathcal{D}	Set of all destination regions
\mathcal{T}	Set of all simulation time-steps
\mathcal{M}_r	Set of all visiting areas of region r
\mathcal{J}_r	Set of all neighbouring regions of region r
\mathcal{K}_{k-W+1}^k	Set of all time-steps in moving horizon window of length W beginning at time-step $k \in \mathcal{T}$
C_{rj}^{MAX}	Maximum interboundary flow capacity between region $r \in \mathcal{R}$ and neighbouring region $j \in \mathcal{J}_r^-$ [veh/h]
ρ_r^C	Critical density of region $r \in \mathcal{R}$ at time-step $k \in \mathcal{T}$ [veh/km]
ρ_r^J	Jam density of region $r \in \mathcal{R}$ at time-step $k \in \mathcal{T}$ [veh/km]
u_r^f	Free-flow of region $r \in \mathcal{R}$ at time-step $k \in \mathcal{T}$ [km/h]
T_s	Simulation time-step length [hours]
l_r	Average road length of region $R \in \mathcal{R}$ [km]
β	Parameter that defines the point where inter boundary capacity starts to decrease
K	Total number of simulation time-steps
T	Total simulation time [hours]
W	Number of time-steps in moving horizon window
p_r	Pre-determined path followed by UAV observing region $r \in \mathcal{R}$
p_r^m	Section of path p_r belonging to visiting area $m \in \mathcal{M}_r$ within region $r \in \mathcal{R}$
\mathbf{D}	Origin-destination matrix $\forall k \in \mathcal{T}$
\mathbf{c}_r	A column vector which maps every time-step $k \in \mathcal{T}$ to a visiting area $m \in \mathcal{M}_r$ within region $r \in \mathcal{R}$

TABLE A2: Table of variables.

Notation	Meaning
$\rho_r(k)$	True density of region $r \in \mathcal{R}$ at time-step $k \in \mathcal{T}$ [veh/km]
$\rho_{rd}(k)$	True density of region $r \in \mathcal{R}$ with destination region $d \in \mathcal{D}$ at time-step $k \in \mathcal{T}$ [veh/km]
$\rho_{rjd}(k)$	True density of region $r \in \mathcal{R}$ to neighbouring region $j \in \mathcal{J}_r$ with destination region $d \in \mathcal{D}$ at time-step $k \in \mathcal{T}$
$u_r(k)$	Average speed of region $r \in \mathcal{R}$ at time-step $k \in \mathcal{T}$ [km/h]
$q_r(k)$	Intended vehicle outflow of region $r \in \mathcal{R}$ at time-step $k \in \mathcal{T}$ [veh/h]
$q_{rd}(k)$	Intended vehicle outflow of region $r \in \mathcal{R}$ with destination region $d \in \mathcal{D}$ at time-step $k \in \mathcal{T}$ [veh/h]
$q_{rjd}(k)$	Intended vehicle outflow from region $r \in \mathcal{R}$ to neighbouring region $j \in \mathcal{J}_r$ with destination region $d \in \mathcal{D}$ at time-step $k \in \mathcal{T}$ [veh/h]
$c_{rj}(k)$	Actual vehicle outflow (transfer flow) from region $r \in \mathcal{R}$ to neighbouring region $j \in \mathcal{J}_r$ at time-step $k \in \mathcal{T}$ [veh/h]
$c_{rjd}(k)$	Actual vehicle outflow (transfer flow) from region $r \in \mathcal{R}$ to neighbouring region $j \in \mathcal{J}_r$ with destination region $d \in \mathcal{D}$ at time-step $k \in \mathcal{T}$ [veh/h]
$\hat{\rho}_r(k)$	Estimated true density of region $r \in \mathcal{R}$ at time-step $k \in \mathcal{T}$ [veh/km]
$\hat{\rho}_{rd}(k)$	Estimated true density of region $r \in \mathcal{R}$ with destination region $d \in \mathcal{D}$ at time-step $k \in \mathcal{T}$ [veh/km]
$\hat{\rho}_{rjd}(k)$	Estimated true density of region $r \in \mathcal{R}$ to neighbouring region $j \in \mathcal{J}_r$ with destination region $d \in \mathcal{D}$ at time-step $k \in \mathcal{T}$
$\hat{q}_{rjd}(k)$	Estimated intended vehicle outflow from region $r \in \mathcal{R}$ to neighbouring region $j \in \mathcal{J}_r$ with destination region $d \in \mathcal{D}$ at time-step $k \in \mathcal{T}$ [veh/h]
$\hat{c}_{rjd}(k)$	Estimated actual vehicle outflow (transfer flow) from region $r \in \mathcal{R}$ to neighbouring region $j \in \mathcal{J}_r$ with destination region $d \in \mathcal{D}$ at time-step $k \in \mathcal{T}$ [veh/h]
$\hat{u}_r(k)$	Estimated average speed of region $r \in \mathcal{R}$ at time-step $k \in \mathcal{T}$ [km/h]
$C_{rj}(\rho_j(k))$	Interboundary flow capacity between region $r \in \mathcal{R}$ and neighbouring region $j \in \mathcal{J}_r^-$ [veh/h]
$v_r^p(k)$	Measurement error for density of region $r \in \mathcal{R}$ at time-step $k \in \mathcal{T}$
$v_r^u(k)$	Measurement error for average speed of region $r \in \mathcal{R}$ at time-step $k \in \mathcal{T}$
$w_{rd}^p(k)$	Process error for density of region $r \in \mathcal{R}$ with destination region $d \in \mathcal{D}$ at time-step $k \in \mathcal{T}$
\mathbf{e}_k	Column vector of all measurement and process errors for time-step k
\mathbf{Q}_k	Covariance matrix of vector \mathbf{e}_k
$D_{rd}(k)$	Number of vehicles entering region $r \in \mathcal{R}$ with destination $d \in \mathcal{D}$ at time-step $k \in \mathcal{T}$

1 REFERENCES

- 2 [1] Seo, T., A. M. Bayen, T. Kusakabe, and Y. Asakura, Traffic state estimation on highway: A
3 comprehensive survey. *Annual Reviews in Control*, Vol. 43, 2017, pp. 128–151.
- 4 [2] Munoz, L., X. Sun, R. Horowitz, and L. Alvarez, Traffic density estimation with the cell
5 transmission model. *Proceedings of the 2003 American Control Conference, 2003.*, Vol. 5,
6 2003, pp. 3750–3755 vol.5.
- 7 [3] Coifman, B., Estimating travel times and vehicle trajectories on freeways using dual loop
8 detectors. *Transportation Research Part A: Policy and Practice*, Vol. 36, 2002, pp. 351–364.
- 9 [4] Schoepflin, T. and D. Dailey, Dynamic camera calibration of roadside traffic management
10 cameras for vehicle speed estimation. *IEEE Transactions on Intelligent Transportation Sys-*
11 *tems*, Vol. 4, No. 2, 2003, pp. 90–98.
- 12 [5] Wang, Y. and M. Papageorgiou, Real-time freeway traffic state estimation based on extended
13 Kalman filter: a general approach. *Transportation Research Part B: Methodological*, Vol. 39,
14 2005, pp. 141–167.
- 15 [6] Sobie, C., Life cycle cost analysis of vehicle detection technologies and their impact on
16 adaptive traffic control systems, 2016.
- 17 [7] Kong, Q.-J., Z. Li, Y. Chen, and Y. Liu, An Approach to Urban Traffic State Estimation by
18 Fusing Multisource Information. *IEEE Transactions on Intelligent Transportation Systems*,
19 Vol. 10, 2009, pp. 499–511.
- 20 [8] Nantes, A., D. Ngoduy, A. Bhaskar, M. Miska, and E. Chung, Real-time traffic state estima-
21 tion in urban corridors from heterogeneous data. *Transportation Research Part C: Emerging*
22 *Technologies*, Vol. 66, 2016, pp. 99–118.
- 23 [9] Kong, Q.-J., Q. Zhao, C. Wei, and Y. Liu, Efficient Traffic State Estimation for Large-Scale
24 Urban Road Networks. *IEEE Transactions on Intelligent Transportation Systems*, Vol. 14,
25 2013, pp. 398–407.
- 26 [10] Herrera, J. C., D. B. Work, R. Herring, X. J. Ban, Q. Jacobson, and A. M. Bayen, Evaluation
27 of traffic data obtained via GPS-enabled mobile phones: The Mobile Century field experi-
28 ment. *Transportation Research Part C: Emerging Technologies*, Vol. 18, 2010, pp. 568–583.
- 29 [11] Butila, E. V. and R. G. Boboc, Urban Traffic Monitoring and Analysis Using Unmanned
30 Aerial Vehicles (UAVs): A Systematic Literature Review. *Remote Sensing*, Vol. 14, 2022.
- 31 [12] Kyrkou, C., S. Timotheou, P. Kolios, T. Theocharides, and C. Panayiotou, Drones: Augment-
32 ing Our Quality of Life. *IEEE Potentials*, Vol. 38, 2019, pp. 30–36.
- 33 [13] Ke, R., Z. Li, S. Kim, J. Ash, Z. Cui, and Y. Wang, Real-Time Bidirectional Traffic Flow
34 Parameter Estimation From Aerial Videos. *IEEE Transactions on Intelligent Transportation*
35 *Systems*, Vol. 18, 2017, pp. 890–901.
- 36 [14] Ke, R., Z. Li, J. Tang, Z. Pan, and Y. Wang, Real-Time Traffic Flow Parameter Estimation
37 From UAV Video Based on Ensemble Classifier and Optical Flow. *IEEE Transactions on*
38 *Intelligent Transportation Systems*, Vol. 20, 2019, pp. 54–64.
- 39 [15] Wang, J., S. Simeonova, and M. Shahbazi, Orientation-and Scale-Invariant Multi-Vehicle
40 Detection and Tracking from Unmanned Aerial Videos. *Remote Sensing*, Vol. 11, 2019.
- 41 [16] Liu, M., L. Tang, and Z. Li, Real-Time Object Detection in UAV Vision based on Neural
42 Processing Units. *2022 IEEE 6th Information Technology and Mechatronics Engineering*
43 *Conference (ITOEC)*, Vol. 6, 2022, pp. 1951–1955.

- 1 [17] Wu, D., D. I. Arkhipov, M. Kim, C. L. Talcott, A. C. Regan, J. A. McCann, and N. Venkata-
- 2 subramanian, ADDSEN: Adaptive Data Processing and Dissemination for Drone Swarms in
- 3 Urban Sensing. *IEEE Transactions on Computers*, Vol. 66, 2017, pp. 183–198.
- 4 [18] Garcia-Aunon, P., J. J. Roldán, and A. Barrientos, Monitoring traffic in future cities with
- 5 aerial swarms: Developing and optimizing a behavior-based surveillance algorithm. *Cogni-*
- 6 *tive Systems Research*, Vol. 54, 2019, pp. 273–286.
- 7 [19] Elloumi, M., R. Dhaou, B. Escrig, H. Idoudi, and L. Saidane, Monitoring road traffic with a
- 8 UAV-based system. *IEEE Wireless Communications and Networking Conference*, 2018, pp.
- 9 1–6.
- 10 [20] Barmponakis, E. and N. Geroliminis, On the new era of urban traffic monitoring with mas-
- 11 sive drone data: The pNEUMA large-scale field experiment. *Transportation Research Part*
- 12 *C: Emerging Technologies*, Vol. 111, 2020, pp. 50–71.
- 13 [21] Kyrkou, C., S. Timotheou, P. Kolios, T. Theocharides, and C. G. Panayiotou, Optimized
- 14 vision-directed deployment of UAVs for rapid traffic monitoring. *2018 IEEE International*
- 15 *Conference on Consumer Electronics (ICCE)*, 2018, pp. 1–6.
- 16 [22] Englezou, Y., S. Timotheou, and C. Panayiotou, Estimating the Origin-Destination Matrix
- 17 using link count observations from Unmanned Aerial Vehicles. In *2021 IEEE International*
- 18 *Intelligent Transportation Systems Conference (ITSC)*, 2021, pp. 3539–3544.
- 19 [23] Englezou, Y., S. Timotheou, and C. Panayiotou, Probabilistic traffic density estimation using
- 20 measurements from Unmanned Aerial Vehicles. In *2022 IEEE International Conference on*
- 21 *Unmanned Aerial Systems (ICUAS)*, 2022, pp. 1381–1388.
- 22 [24] Ramezani, M., J. Haddad, and N. Geroliminis, Dynamics of heterogeneity in urban net-
- 23 works: aggregated traffic modeling and hierarchical control. *Transportation Research Part*
- 24 *B: Methodological*, Vol. 74, 2015, pp. 1–19.
- 25 [25] Yildirimoglu, M., M. Ramezani, and N. Geroliminis, Equilibrium Analysis and Route Guid-
- 26 ance in Large-scale Networks with MFD Dynamics. *Transportation Research Procedia*,
- 27 Vol. 9, 2015, pp. 185–204.
- 28 [26] Wagter, C. D., B. Remes, E. Smeur, F. van Tienen, R. Ruijsink, K. van Hecke, and E. van der
- 29 Horst, The NederDrone: A hybrid lift, hybrid energy hydrogen UAV. *International Journal*
- 30 *of Hydrogen Energy*, Vol. 46, 2021, pp. 16003–16018.
- 31 [27] Menelaou, C., S. Timotheou, P. Kolios, and C. G. Panayiotou, Joint Route Guidance and De-
- 32 mand Management for Real-Time Control of Multi-Regional Traffic Networks. *IEEE Trans-*
- 33 *actions on Intelligent Transportation Systems*, 2021.
- 34 [28] Grandinetti, P., C. Canudas-de Wit, and F. Garin, Distributed Optimal Traffic Lights Design
- 35 for Large-Scale Urban Networks. *IEEE Transactions on Control Systems Technology*, Vol. 27,
- 36 No. 3, 2019, pp. 950–963.
- 37 [29] Menelaou, C., S. Timotheou, P. Kolios, and C. G. Panayiotou, Joint Route Guidance and De-
- 38 mand Management for Real-Time Control of Multi-Regional Traffic Networks. *IEEE Trans-*
- 39 *actions on Intelligent Transportation Systems*, Vol. 23, No. 7, 2022, pp. 8302–8315.
- 40 [30] Menelaou, C., S. Timotheou, P. Kolios, C. G. Panayiotou, and M. M. Polycarpou, Mini-
- 41 mizing Traffic Congestion Through Continuous-Time Route Reservations With Travel Time
- 42 Predictions. *IEEE Transactions on Intelligent Vehicles*, Vol. 4, No. 1, 2019, pp. 141–153.
- 43 [31] Menelaou, C., S. Timotheou, P. Kolios, and C. G. Panayiotou, Improved Road Usage Through
- 44 Congestion-Free Route Reservations. *Transportation Research Record*, Vol. 2621, No. 1,
- 45 2017, pp. 71–80.

- 1 [32] Menelaou, C., P. Kolios, S. Timotheou, C. Panayiotou, and M. Polycarpou, Controlling road
2 congestion via a low-complexity route reservation approach. *Transportation Research Part*
3 *C: Emerging Technologies*, Vol. 81, 2017, pp. 118–136.
- 4 [33] Kerner, B. S., The maximization of the network throughput ensuring free flow condi-
5 tions in traffic and transportation networks: Breakdown minimization (BM) principle versus
6 Wardrop’s equilibria. *The European Physical Journal B*, Vol. 89, No. 9, 2016, p. 199.
- 7 [34] Makrigiorgis, R., P. Kolios, S. Timotheou, T. Theocharides, and C. Panayiotou, Extracting the
8 fundamental diagram from aerial footage. *2020 IEEE 91st Vehicular Technology Conference*,
9 2020, pp. 1–5.